Supplementary Information: Two-field stability control of marginally stable magnetorheological elastomers

E. Psarra[†], L. Bodelot[†], and K. Danas[*†]

[†]LMS, C.N.R.S., École Polytechnique, Université Paris-Saclay, 91128 Palaiseau, France

Abstract

We give more details on the experimental procedure and we derive in detail the first and second variations of the potential energy used to carry out the numerical simulations. The numerical part is presented in a comprehensive way and allows direct implementation in standard (commercial and non-commercial) finite element codes. We also investigate in depth the effect of friction on the lateral faces between the magnetorheological film/substrate system and the experimental setup used to apply pre-compression. We find that friction can have very significant effects on the obtained response and the present numerical analysis explains a number of results obtained experimentally.

1 Experimental procedure and image processing

The compression device is 3D-printed in a polymeric material so as not to interfere with the magnetic field during the experiments. It consists of three orthogonal walls forming a U shape (Fig.S1). A non-magnetic screw-driven system is used to control the distance between the two parallel walls and thus defines the applied pre-compression stretch ratio λ_0. Before compression, silicone oil is applied onto the lateral faces of the film/substrate block that is in contact with the setup walls to decrease friction. Even so at large pre-compressions, friction effects are not negligible and need to be taken into account in the numerical analysis to reach a good quantitative agreement with experiments (see Section 3). In turn, the bottom part of the block is uncoated in order to prevent pronounced translations at the bottom of the substrate. The specimens are magnetically and mechanically unloaded and then retested under an increased pre-compression value. It is important to specify that the specimens have been pre-cycled mechanically and magnetically to reach a stabilized state before recording the experimental data.

The entire system is subsequently installed with the MRE layer perpendicular to the magnetic field, within the 82 mm-air gap separating the two 90 mm-diameter poles of a two-coil electromagnet, as seen in Fig.S1. The magnetic field is increased linearly from 0 to 0.6T at a rate of 0.002 T/s. An external sensor is used to measure the amplitude of the applied magnetic field as far as possible from the boundary of the film/substrate block.

The bifurcation curves are then obtained by image processing of 12 μm/pixel resolution images, which were recorded during testing at a rate of 17 frames per 0.1T magnetic field increment. Due to the tight spacing of the magnetic poles the current setup does not allow the direct visualization and measurement of the wrinkling from the top of the film. Future work in different setups is underway and will allow quantitative analysis of more complex magneto-mechanical wrinkling patterns such as those obtained for small pre-compressions (see inset of blue region in Fig.5b of the main article).

We process the digital images in Matlab in order to obtain the bifurcation amplitude A curves of several specimens under the range of pre-compressions $\lambda_0 \in [0.7, 0.98]$ tested. Grayscale images (e.g., Fig.3a-p) are first normalized so that pixel values in the range of [0,1] represented their brightness. In order to detect the film profile evolution versus the applied magnetic field, the contrast between the dark film and the light background is enhanced by binarizing the images. In particular, after setting a threshold (~ 0.3) defining whether a pixel intensity corresponds to the film or to the lighter background close to the film, the position vector of the pixels located at the film/background interface (jump from 1 to 0) is stored for the initial (i.e., zero magnetic field) and magnetically loaded film configurations. We consider that clear wrinkling occurs away from the boundaries and thus both edge wrinkles are excluded from the bifurcation analysis. The absolute amplitude of the edge wrinkles tends to be higher due to friction effects (see discussion in Section 3), as well as due to magnetic field concentration near the corners of the specimen (as shown in the contours of Fig.6). The global maximum (peak) and minimum (valley) of the central wrinkles are then tracked and the corresponding vertical displacements u_2 (along the field direction) are measured from the trajectories of the extreme points. The amplitude of film deflection A is quantified as the average distance between the peak and the valley of the two wrinkles (Fig.S2). The pixel coordinate system is then transformed into the laboratory Cartesian system. The difference between the current amplitude A at given magnetic field b_0 and the initial (reference) film amplitude A_0, i.e. $A - A_0$, is evaluated, e.g., Figs.3q,5a. The same process is also followed to obtain the numerical bifurcation curves as discussed in the next section.

*Corresponding author: konstantinos.danas@polytechnique.edu

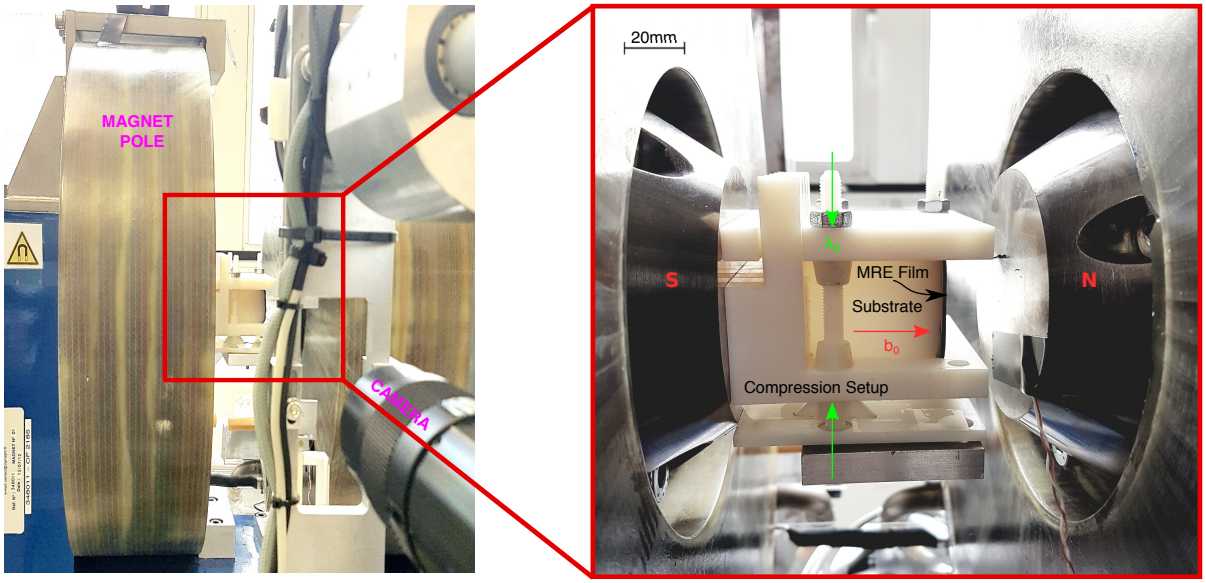

Figure S1 Custom-made setup for the magnetomechanical experiment. The specimens are uniaxially compressed at a given stretch λ_0 with a non-magnetic screw-driven device. The pre-compression is fixed and the system enters within the two poles of the electromagnet. The magnetic loading (b_0) is applied along the film thickness in a linearly increasing fashion. A camera records the profile of the specimen and thus the wrinkling of the film.

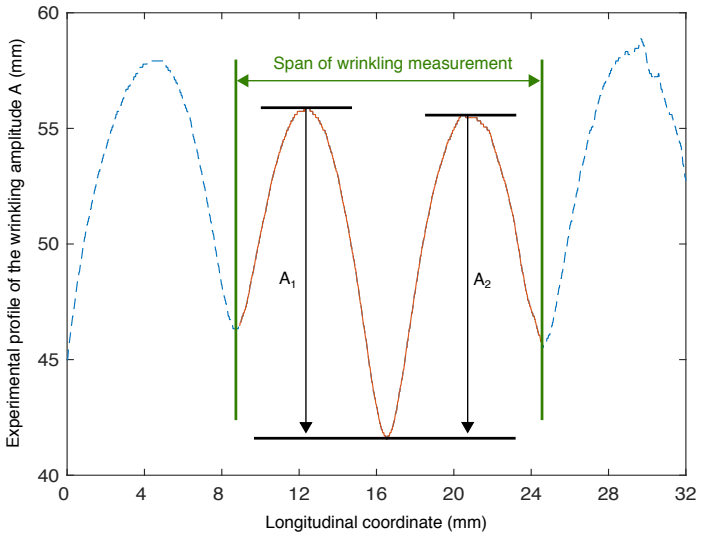

Figure S2 Detection of the film-background interface corresponding to the film profile at $\lambda_0 = 0.8$ and $b_0 = 0.2$T. Our image analysis excludes the external wrinkles to avoid measurements affected by friction. The current amplitude of film deflection A is determined as the average value of the two middle wrinkle amplitudes, $A = (A_1 + A_2)/2$.

2 Variational formulation for finite magnetoelasticity

In this section, we discuss the variational formulation used in the finite element algorithms and explicit expressions are given for the first variation (i.e., force vector), which yields the equilibrium and Maxwell equations, and the second variation (i.e. stiffness matrix) of the variational principle. First, we consider the potential energy [1] (but see also [2,3]) neglecting mechanical body forces:

$$\mathscr{P}(\mathbf{u},\mathbf{A}) = \int_{\Omega_i} \rho_0^i \Phi_i(\mathbf{F},\mathbf{B})\,\mathrm{d}\Omega + \int_{\Re^3} \frac{1}{2\mu_0 J}\,\|\mathbf{F}\cdot\mathbf{B}\|^2\,\mathrm{d}\Omega - \int_{\partial\Omega_i^t} \mathbf{T}\cdot\mathbf{u}\,dS, \tag{1}$$

Here, $\|.\|$ is the standard Euclidean norm, while $\mathbf{B}$ (with $\mathbf{b} = J^{-1}\mathbf{F}\mathbf{B}$) and $\mathbf{A}$ (with $\mathbf{B} = \nabla\times\mathbf{A} \equiv \mathrm{Curl}\mathbf{A}$) are Lagrangian vectors. The deformation gradient $\mathbf{F} = \nabla\mathbf{x} = \mathbf{I} + \nabla\mathbf{u}$ (we use standard notation $\nabla \equiv \mathrm{Grad}$ in the reference configuration) is a two-point tensor describing the transformation of a material point from the reference to the deformed configuration. Note also the determinant $J = \det\mathbf{F} > 0$, with $\mathbf{x} = \mathbf{X} + \mathbf{u}(\mathbf{X})$ denoting the position vector of a material point in the deformed configuration, $\mathbf{X}$ the position vector of the same point in the reference configuration and $\mathbf{u}$ the displacement vector. In turn, the Helmholtz free energy density Φ_i depends on the material choice, with $i = f,s$ for the film and the substrate, respectively. In addition, ρ_0^i is the reference density such that the current density reads by $\rho_0^i = \rho^i J$. It is noted here that in order to model the air domain,

it suffices to set $\rho_0^{air} = 0$. As a consequence, all subsequent expressions are valid for all phases (MRE film, substrate and air). In this regard, the second term in (1) serves to describe the background magnetic (Maxwell) energy in the entire space $\Re^3$ and thus it accounts for all three phases, i.e., film, substrate and air. $\mathbf{T}$ is the mechanical surface traction vector applied at the traction part of the boundary of the reference volume denoted with $\partial\Omega_i^t$.

2.1 First variation and force vector

In equation (1), $\mathbf{u}$ and $\mathbf{A}$ serve as independent variables with respect to which the potential energy in (1) is minimized. This is achieved first by considering the first and second variations of $\mathscr{P}$ with respect to the independent variables. The first variation simply reads

$$\delta\mathscr{P}(\mathbf{u},\mathbf{A}) = \mathscr{P}_{,\mathbf{u}}\,\delta\mathbf{u} + \mathscr{P}_{,\mathbf{A}}\,\delta\mathbf{A}. \tag{2}$$

To be more specific, it is helpful to define the following variations, where $\mathbf{C} = \mathbf{F}^T\cdot\mathbf{F}$ denotes the right Cauchy-Green tensor such that[1]

$$\begin{aligned}
&\delta\mathbf{F} = \delta\mathbf{u}\nabla, \qquad \delta\mathbf{C} = 2\mathbf{F}^T\cdot(\delta\mathbf{u}\nabla), \qquad \delta\mathbf{B} = \nabla\times\delta\mathbf{A}\\
&\delta\rho = -\rho\,\mathbf{F}^{-T}:(\delta\mathbf{u}\nabla), \qquad \delta\left(J^{-1}\right) = -J^{-1}\,\mathbf{F}^{-T}:(\delta\mathbf{u}\nabla) = \frac{\delta\rho}{\rho_0}.
\end{aligned} \tag{3}$$

Then, dropping for simplicity the indexes i referring to material properties and using (2) together with (3), one gets

$$\begin{aligned}
\delta\mathscr{P} = &\int_\Omega \rho_0\left\{\frac{\partial\Phi}{\partial\mathbf{F}}:(\delta\mathbf{u}\nabla) + \frac{\partial\Phi}{\partial\mathbf{B}}\cdot(\nabla\times\delta\mathbf{A})\right\}\mathrm{d}\Omega\\
&+\int_{\Re^3}\left\{\frac{\delta\left(J^{-1}\right)}{2\mu_0}(\nabla\times\mathbf{A})\cdot\mathbf{C}\cdot(\nabla\times\mathbf{A}) + \frac{1}{\mu_0 J}(\nabla\times\mathbf{A})\cdot\mathbf{C}\cdot(\nabla\times\delta\mathbf{A})\right.\\
&\left.+\frac{1}{2\mu_0 J}(\nabla\times\mathbf{A})\cdot\delta\mathbf{C}\cdot(\nabla\times\mathbf{A})\right\}\mathrm{d}\Omega - \int_{\partial\Omega^t}\mathbf{T}\cdot\delta\mathbf{u}\,\mathrm{d}S,
\end{aligned} \tag{4}$$

which can be rewritten in terms of $\delta\mathbf{F}$ and $\delta\mathbf{B}$ by use of definitions (3) as

$$\begin{aligned}
\delta\mathscr{P} = &\int_\Omega \rho_0\left\{\frac{\partial\Phi}{\partial\mathbf{F}}:\delta\mathbf{F} + \frac{\partial\Phi}{\partial\mathbf{B}}\cdot\delta\mathbf{B}\right\}\mathrm{d}\Omega\\
&+\int_{\Re^3}\left\{-\frac{1}{2\mu_0 J}\|\mathbf{F}\cdot\mathbf{B}\|^2\,\mathbf{F}^{-T}:\delta\mathbf{F} + \frac{1}{\mu_0 J}(\mathbf{F}\cdot\mathbf{B})\cdot[\mathbf{F}\cdot(\delta\mathbf{B})] + \frac{1}{\mu_0 J}[(\mathbf{F}\cdot\mathbf{B})\,\mathbf{B}]:\delta\mathbf{F}\right\}\mathrm{d}\Omega\\
&-\int_{\partial\Omega_m^t}\mathbf{T}\cdot\delta\mathbf{u}\,\mathrm{d}S.
\end{aligned} \tag{5}$$

Next, gathering the variations with respect to $\delta\mathbf{F}$ and $\delta\mathbf{B}$ one obtains the following quantities in index notation

$$\begin{aligned}
&\frac{\partial\mathscr{P}}{\partial F_{ij}} = \rho_0\frac{\partial\Phi}{\partial F_{ij}} - \frac{1}{2\mu_0 J}\|\mathbf{F}\cdot\mathbf{B}\|^2\,F_{ji}^{-1} + \frac{1}{\mu_0 J}F_{ir}B_rB_j \quad (\text{in } \Re^3),\\
&\frac{\partial\mathscr{P}}{\partial B_i} = \rho_0\frac{\partial\Phi}{\partial B_i} + \frac{1}{\mu_0 J}F_{rk}B_kF_{ri} \quad (\text{in } \Re^3).
\end{aligned}$$

2.2 Second variation and Jacobian matrix

Similarly, the second variation of the potential energy (1), which forms the Jacobian of the numerical system of equations can be written in the form

$$\Delta\delta\mathscr{P} = (\mathscr{P}_{,\mathbf{uu}}\Delta\mathbf{u})\,\Delta\mathbf{u} + \left(\mathscr{P}_{,\mathbf{Au}}\Delta\mathbf{A}\right)\Delta\mathbf{u} + \left(\mathscr{P}_{,\mathbf{uA}}\Delta\mathbf{u}\right)\Delta\mathbf{A} + \left(\mathscr{P}_{,\mathbf{AA}}\Delta\mathbf{A}\right)\Delta\mathbf{A}, \tag{6}$$

or in matrix notation (and by use of definitions (3)) as

$$\Delta\delta\mathscr{P} = \{\Delta\mathbf{F},\Delta\mathbf{B}\}\begin{bmatrix}\dfrac{\partial^2\mathscr{P}}{\partial\mathbf{F}\partial\mathbf{F}} & \dfrac{\partial^2\mathscr{P}}{\partial\mathbf{F}\partial\mathbf{B}}\\[2ex] \dfrac{\partial^2\mathscr{P}}{\partial\mathbf{B}\partial\mathbf{F}} & \dfrac{\partial^2\mathscr{P}}{\partial\mathbf{B}\partial\mathbf{B}}\end{bmatrix}\begin{Bmatrix}\delta\mathbf{F}\\[2ex]\delta\mathbf{B}\end{Bmatrix}. \tag{7}$$

[1] We use the following vector-tensor product notation. For two second-order tensors, $\mathbf{A}$ and $\mathbf{B}$, we define the operations $\mathbf{A}\cdot\mathbf{B} = A_{ik}B_{kj}$, $\mathbf{A}:\mathbf{B} = A_{ij}B_{ij}$. For a second-order tensor $\mathbf{A}$ and a vector $\mathbf{v}$, we denote $\mathbf{A}\cdot\mathbf{v} = A_{ij}v_j$, $\mathbf{v}\mathbf{v} = v_iv_j$ and $\mathbf{v}\cdot\mathbf{v} = v_iv_i$.

The above second-order derivatives are evaluated by direct derivation of the potential energy (1), such that

$$\frac{\partial^2 \mathscr{P}}{\partial F_{ij}\partial F_{kl}} = \rho_0 \frac{\partial^2 \Phi}{\partial F_{ij}\partial F_{kl}} + \frac{1}{2\mu_0 J}\,\|\mathbf{F}\cdot\mathbf{B}\|^2 \left[F^{-1}_{lk}F^{-1}_{ji} - F^{-1}_{jk}F^{-1}_{li}\right] - \frac{1}{\mu_0 J}\left[F_{ks}B_sB_lF^{-1}_{ji} + F_{in}B_nF^{-1}_{lk}B_j - \delta_{ik}B_lB_j\right] \quad (\text{in } \Re^3). \tag{8}$$

and

$$\frac{\partial^2 \mathscr{P}}{\partial F_{ij}\partial B_k} = \rho_0 \frac{\partial^2 \Phi}{\partial F_{ij}\partial B_k} + \frac{1}{\mu_0 J}\left[F_{ik}B_j + F_{in}B_n\delta_{jk} - C_{kr}B_rF^{-1}_{ji}\right] \quad (\text{in } \Re^3), \tag{9}$$

and

$$\frac{\partial^2 \mathscr{P}}{\partial B_i\partial B_j} = \rho_0 \frac{\partial^2 \Phi}{\partial B_i\partial B_j} + \frac{1}{\mu_0 J}C_{ij} \quad (\text{in } \Re^3). \tag{10}$$

2.3 Finite Element Discretization in two-dimensions

One can discretize the above equations by discretizing the total volume Ω in N_e discrete finite elements (and N_n nodes) by

$$\Omega = \sum_{I=1}^{N_e} \Omega_e^I, \tag{11}$$

with Ω_e^I denoting the volume of each element. Then, the element vector of unknowns $\delta\mathbf{q}_e$ is given readily by

$$\delta\mathbf{q}_e = \{\delta\mathbf{u}, \delta\mathbf{A}\}. \tag{12}$$

Next, we define (in a general fashion) the discretized form of the unknown variables, i.e., $\mathbf{u}$ and $\mathbf{A}$, using standard notation

$$\delta\mathbf{u} = \mathbf{N}_u \cdot \delta\mathbf{q}_e, \qquad \delta\mathbf{A} = \mathbf{N}_\alpha \cdot \delta\mathbf{q}_e, \tag{13}$$

where $\mathbf{N}_{q_e}$ are the matrices associated with the element shape functions, whereas in order to compute the gradients, we have

$$\delta\mathbf{u}\nabla = \mathbf{G}_u \cdot \delta\mathbf{q}_e, \qquad \nabla\times\delta\mathbf{A} = \mathbf{G}_\alpha \cdot \delta\mathbf{q}_e, \tag{14}$$

with $\mathbf{G}_{q_e}$ denoting the gradient of the $\mathbf{N}_{q_e}$ matrices. This allows for the definition of the element force vector $\mathbf{f}_e$ conjugate to the element vector of unknowns $\delta\mathbf{q}_e$ and is given readily by

$$\mathbf{f}_e \cdot \delta\mathbf{q}_e = \int_{\Omega_e} \delta\mathscr{P}\,\mathrm{d}\Omega = \left[\int_{\Omega_e}\left\{\frac{\partial\mathscr{P}}{\partial\mathbf{F}} : \mathbf{G}_u + \frac{\partial\mathscr{P}}{\partial\mathbf{B}}\cdot\mathbf{G}_\alpha\right\}\mathrm{d}\Omega\right]\cdot\delta\mathbf{q}_e. \tag{15}$$

Similarly, the element stiffness matrix $\mathbf{k}_e$ is defined by

$$\Delta\mathbf{q}_e\cdot\mathbf{k}_e\cdot\delta\mathbf{q}_e = \int_{\Omega_e}\Delta\delta\mathscr{P}\,\mathrm{d}\Omega = \Delta\mathbf{q}_e\cdot\left\{\int_{\Omega_e}\begin{bmatrix}\mathbf{G}_u^T & \mathbf{G}_\alpha^T\end{bmatrix}\begin{bmatrix}\dfrac{\partial^2\mathscr{P}}{\partial\mathbf{F}\partial\mathbf{F}} & \dfrac{\partial^2\mathscr{P}}{\partial\mathbf{F}\partial\mathbf{B}} \\ \dfrac{\partial^2\mathscr{P}}{\partial\mathbf{B}\partial\mathbf{F}} & \dfrac{\partial^2\mathscr{P}}{\partial\mathbf{B}\partial\mathbf{B}}\end{bmatrix}\begin{bmatrix}\mathbf{G}_u \\ \mathbf{G}_\alpha\end{bmatrix}\mathrm{d}\Omega\right\}\cdot\delta\mathbf{q}_e. \tag{16}$$

We write the force vector and stiffness matrix in index notation and we define the local-to-global coordinate transformation by the Jacobian matrix, denoted as $[\mathscr{J}] = \partial X_i/\partial\xi_j = \sum_{I=1}^{N_n}(\partial N_I/\partial\xi_j)X_i^I$, $i = 1,2$, pertinent to the shape functions N. Subsequently, we evaluate the quantities $\mathbf{u}\nabla$ and $\nabla\times\mathbf{A}$ by

$$\underbrace{\begin{bmatrix}\partial u_1/\partial X_1 \\ \partial u_1/\partial X_2 \\ \partial u_2/\partial X_1 \\ \partial u_2/\partial X_2 \\ \partial A_3/\partial X_2 \\ -\partial A_3/\partial X_1\end{bmatrix}}_{[\mathbf{dqdx}]} = \underbrace{\begin{bmatrix}\mathscr{J}^{-1}_{11} & \mathscr{J}^{-1}_{12} & 0 & 0 & 0 & 0 \\ \mathscr{J}^{-1}_{21} & \mathscr{J}^{-1}_{22} & 0 & 0 & 0 & 0 \\ 0 & 0 & \mathscr{J}^{-1}_{11} & \mathscr{J}^{-1}_{12} & 0 & 0 \\ 0 & 0 & \mathscr{J}^{-1}_{21} & \mathscr{J}^{-1}_{22} & 0 & 0 \\ 0 & 0 & 0 & 0 & \mathscr{J}^{-1}_{21} & \mathscr{J}^{-1}_{22} \\ 0 & 0 & 0 & 0 & -\mathscr{J}^{-1}_{11} & -\mathscr{J}^{-1}_{12}\end{bmatrix}}_{[\mathbf{JI}]}\underbrace{\begin{bmatrix}\partial u_1/\partial\xi_1 \\ \partial u_1/\partial\xi_2 \\ \partial u_2/\partial\xi_1 \\ \partial u_2/\partial\xi_2 \\ \partial A_3/\partial\xi_1 \\ \partial A_3/\partial\xi_2\end{bmatrix}}_{[\mathbf{dqdxi}]}, \tag{17}$$

and the vector **dqdxi** by

$$\underbrace{\begin{bmatrix} \partial u_1/\partial \xi_1 \\ \partial u_1/\partial \xi_2 \\ \partial u_2/\partial \xi_1 \\ \partial u_2/\partial \xi_2 \\ \partial A_3/\partial \xi_1 \\ \partial A_3/\partial \xi_2 \end{bmatrix}}_{[\mathbf{dqdxi}]} = \underbrace{\begin{bmatrix} \mathscr{G}_{11} & 0 & 0 & \mathscr{G}_{21} & 0 & 0 & \mathscr{G}_{31} & 0 & 0 & \mathscr{G}_{41} & 0 & 0 \\ \mathscr{G}_{12} & 0 & 0 & \mathscr{G}_{22} & 0 & 0 & \mathscr{G}_{32} & 0 & 0 & \mathscr{G}_{42} & 0 & 0 \\ 0 & \mathscr{G}_{11} & 0 & 0 & \mathscr{G}_{21} & 0 & 0 & \mathscr{G}_{31} & 0 & 0 & \mathscr{G}_{41} & 0 \\ 0 & \mathscr{G}_{12} & 0 & 0 & \mathscr{G}_{22} & 0 & 0 & \mathscr{G}_{32} & 0 & 0 & \mathscr{G}_{42} & 0 \\ 0 & 0 & \mathscr{G}_{11} & 0 & 0 & \mathscr{G}_{21} & 0 & 0 & \mathscr{G}_{31} & 0 & 0 & \mathscr{G}_{41} \\ 0 & 0 & \mathscr{G}_{12} & 0 & 0 & \mathscr{G}_{22} & 0 & 0 & \mathscr{G}_{32} & 0 & 0 & \mathscr{G}_{42} \end{bmatrix}}_{[\mathbf{NG}]} \underbrace{\begin{bmatrix} u_1^{(1)} \\ u_2^{(1)} \\ A^{(1)} \\ u_1^{(2)} \\ u_2^{(2)} \\ A^{(2)} \\ u_1^{(3)} \\ u_2^{(3)} \\ A^{(3)} \\ u_1^{(4)} \\ u_2^{(4)} \\ A^{(4)} \end{bmatrix}}_{\mathbf{q}_e} . \tag{18}$$

Then, the derivative matrix $[\mathbf{G}]$ is given by

$$[\mathbf{G}] = [\mathbf{G}_u \quad \mathbf{G}_\alpha] = [\mathbf{JI}]\,[\mathbf{NG}]\,. \tag{19}$$

2.4 Mesh and boundary conditions

To solve the boundary value problem of a finite geometry in nonlinear magnetoelasticity, we implement the above described magnetoelastic element in the general code FEAP[4]. We define a simple, but largely sufficient, plane-strain 4-node quadrilateral isoparametric element, with 3 degrees of freedom per node: the displacements $\mathbf{u} = \{u_1(X_1,X_2), u_2(X_1,X_2)\}$ and the magnetic vector potential $\alpha = A_3(X_1,X_2)$, with (X_1,X_2) the global reference coordinates. The (A_1,A_2) components are zero since $\mathbf{B} = \{B_1,B_2,0\} = \{\partial A_3/\partial X_2, -\partial A_3/\partial X_1, 0\}$ (we remind that $\mathbf{B} = \nabla \times \mathbf{A}$). The nodal unknowns $\mathbf{q}_e \equiv \{\delta u_1, \delta u_3, \delta\alpha\}$ were interpolated by $\delta q_i(X_1,X_2) = \sum_{j=1}^{4} \delta q_i^j N_j(X_1,X_2)$ (with δq_i^j denoting the 4 nodal values of the degrees of freedom), using linear shape functions,

$$\begin{aligned} N_1(\xi_1,\xi_2) &= \frac{1}{4}(1-\xi_1)(1-\xi_2), \qquad & N_2(\xi_1,\xi_2) &= \frac{1}{4}(1-\xi_1)(1+\xi_2), \\ N_3(\xi_1,\xi_2) &= \frac{1}{4}(1+\xi_1)(1+\xi_2), \qquad & N_4(\xi_1,\xi_2) &= \frac{1}{4}(1+\xi_1)(1-\xi_2), \end{aligned} \tag{20}$$

with $(\xi_1,\xi_2) \in [-1,1]$ denoting the local coordinates.

Following convergence studies, the number of elements in the film is 1200, in the substrate 5200 and in the air 10160. The nonlinear solutions of the field equations are obtained incrementally with the use of a standard Newton-Raphson scheme. In turn, the air domain needs special treatment, since it has no mechanical energy and thus the deformation gradient is undefined therein. In view of this, we have partitioned the air mesh into two domains. One with a structured mesh and the rest with unstructured mesh, as shown in Fig.S3.

Specifically, the first structured domain is deformable and spatially defined by a square of side length $2R_f + L$, concentric to the solid square of side length $L(= 40\text{mm})$. We use $R_f = 0.5\Delta L_{air}$, where ΔL_{air} is the half length size of the entire air domain minus the solid domain (see Fig.S3). The elements within the deformable air domain are forced to deform to avoid severe mesh distortion near the specimen/air interface. This fictitious air deformation does not alter the solution of the problem since the air density is zero and thus does not contribute to the mechanical energy of the system. To achieve this fictitious deformation, we follow the steps below:

(i) for all nodes lying in the deformable air domain, we find the closest node on the specimen boundary by a simple search algorithm, thus defining a set of pairs of size N_{a-s}.

(ii) for each pair of air-solid nodes, we define the linear constraint function $c_u = (1 - |x_i^{(2)} - x_i^{(1)}|/R_f) \cdot u_i^{(2)} - u_i^{(1)} = 0$, with $i = 1,2$. In this last expression, node (1) belongs to the deformable air and node (2) to the solid domain, respectively.

(iii) the above constraint function can be achieved with either a Lagrange multiplier or a penalty formulation. For simplicity, we choose the second option and we define the penalty energy

$$\Phi_{pen}(u_i) = \sum_{n=1}^{N_{a-s}} \sum_{i=1}^{2} \frac{1}{2\varepsilon} \left[\left(1 - \frac{|x_i^{(n,solid)} - x_i^{(n,air)}|}{R_f} \right) u_i^{(n,solid)} - u_i^{(n,air)} \right]^2 \tag{21}$$

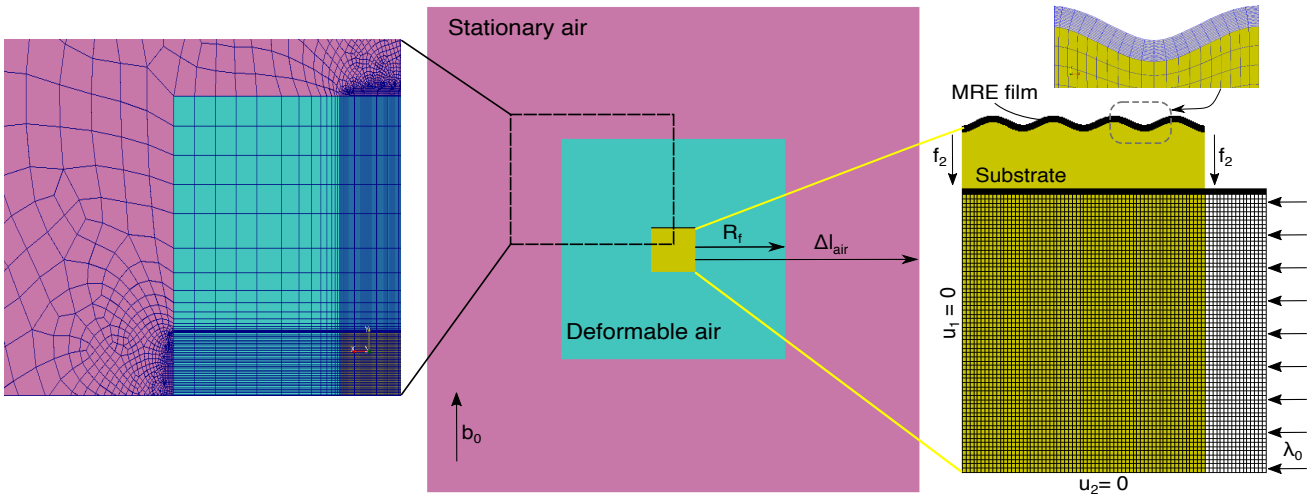

Figure S3 Mesh of the film/substrate/air system. All regions are meshed with quadrilateral bilinear, 4-node isoparametric, magnetomechanical elements. A structured mesh (blue) with deformable elements is defined by the distance R_f from the solid boundary. The rest of the air region (purple) (defined by distance Δl_{air} from the solid boundary) is unstructured and stationary.

which is added to the original variational formulation (1).

(iv) we choose a sufficiently small value for $\varepsilon = 10^{-7}$ such that the constraint function is satisfied to a good accuracy. This value and approach leads in general to more accurate results and better convergence than that of using a small but finite shear and bulk moduli for the air domain.

(v) we consider first and second variations in (21) with respect to u_i and amend the original force vector and stiffness matrix of the entire system.

Finally, for the undeformable air domain, we apply identically zero displacements $u_i = 0$ $(i = 1,2)$. In turn, the magnetic field is applied via the vector potential α[5] by imposing at the outer boundary of the air the following condition

$$\alpha(X_1,X_2) = \varepsilon_{ij}(B_0)_i X_j, \qquad X_i \in \partial\Re^3, \qquad \mathbf{B}_0 = \mathbf{b}_0. \tag{22}$$

In the above equation, we have abused the notation $\Re^3$ to denote the boundary of the undeformable (outer) air domain. In addition, the Lagrangian, $\mathbf{B}_0$, and Eulerian, $\mathbf{b}_0$, magnetic fields are equal in the stationary air domain by definition.

3 Friction effects due to high pre-compression

In this section, we analyze numerically the response of the MRE film/substrate system at large pre-compressions $\lambda_0 \in [0.7, 0.78]$ and probe the relevant experimental results. This study has as a goal to understand better the absence of wrinkling for purely mechanical pre-compressions, i.e., $b_0 = 0$, $\lambda_0 < 1$, even beyond the purely mechanical bifurcation point $\lambda_0^c = 0.76$, which has been obtained numerically for the ratio $G_s/G_f = 0.3$.

We begin the analysis by first noting in Fig.3a,e,i,m a noticeable curvature at the corners of the film. This curvature grows as a function of pre-compression and is obviously related to friction effects at the boundary between the film/substrate and the compression setup, even after silicone oil is applied onto the lateral faces that are in contact. The resulting curvature is not negligible when compared with the thickness of the MRE film and the size of the specimen. As we show numerically, the presence of friction and the resulting curvature inhibit a clean mechanical wrinkling instability and lead to a combined wrinkle and localized pre-crease pattern.

In order to model numerically the friction effect, and taking into account the complexity of the air modeling as well as the partial continuity of the magnetic fields, we employ an approximate procedure that does not necessitate the direct modeling of contact. Specifically, we bypass the contact problem by adding an empirical tangential force f_2 (in the X_2 direction) at the lateral edges of the block (see Fig.2 in the main text) to mimic contact. This force is a function of the applied pre-compression λ_0 and reads

$$f_2 = f_{max}\,\frac{1-\lambda_0}{1-\lambda_0^{max}}, \qquad f_{max} = 72\mu N, \quad \lambda_0^{max} = 0.73. \tag{23}$$

The quantity λ_0^{max} corresponds to the maximum pre-compression achieved experimentally. The previous law is related to a nonlinear friction law in the sense that the applied stretch in direction X_1, i.e. $\lambda_0 \equiv \lambda_1$ is related in a nonlinear fashion to the normal force f_1 at the lateral face. The maximum force f_{max} constitutes then a simple fitting parameter which is obtained by fitting the early stage of the post-bifurcation response at $\lambda_0 = 0.73$.

In Fig.S4a, we examine quantitatively the effect of friction upon the bifurcation amplitude for three pre-compressions, $\lambda_0 = 0.73, 0.75, 0.78$. The main observation in this figure is that by application of friction (continuous curves denoted with "W/ friction"), the bifurcation transition stagnates and does not further decrease with increase of pre-compression (i.e. decrease of λ_0). By contrast, when the numerical calculations are frictionless, the curves exhibit a strong dependence on λ_0. For sufficiently small $\lambda_0 = 0.73$, the numerical film/substrate wrinkles and develops a non-zero amplitude well before the application of the magnetic field b_0. There is of course a transition point, which is directly linked to the purely mechanical critical wrinkling load, which is $\lambda_0^c = 0.76$. In this case, the bifurcation curve would start exactly at the origin in Fig.S4a (not shown here). This observation implies that by reducing friction and hence boundary effects one can achieve wrinkling via a critical magnetic field that is very close to zero, i.e. $b_0^c \sim 0$T, as theoretically suggested in[3]. That is a significant point that deserves further investigation and will be addressed in a future work.

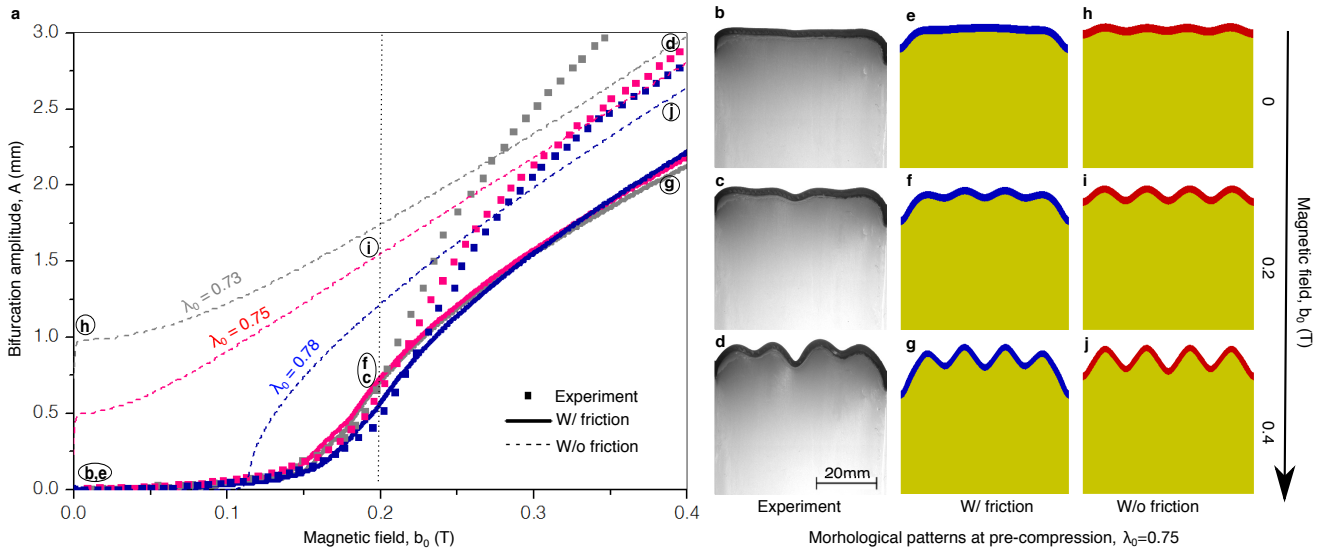

Figure S4 Role of lateral friction on critical loads and patterns for high pre–compressions λ_0. Friction is modeled by applying a tangential force $f_2 = 72\mu$N along X_2 direction at the lateral edges of the two-dimensional solid. **a**) Comparison between the experimental bifurcation curves (symbols) vs. numerical curves with and without friction (continuous and dashed lines respectively) for $\lambda_0 = 0.73, 0.75, 0.78$; (**b-d**) Experimental and (**e-j**) numerical morphological modes with friction (film in blue) and without friction (film in red), respectively. At high pre-compression $\lambda_0 = 0.75 < \lambda_0^c$ and in the presence of friction (**e**), the mechanical wrinkling mode vanishes but not in the case without friction (**h**); The numerical pattern with friction turns into a more localized configuration (**g**), which fits better the experimental period-doubling and localized (pre-crease) morphology (**d**) than the numerical pattern without friction (**j**).

For completeness, the influence of friction on the critical modes is also depicted in Fig.S4b-j. Here, we compare qualitatively the experimental morphological pattern evolution (Fig.S4b-d) versus the numerical results with (Fig.S4e-g) and without (Fig.S4h-j) friction for $\lambda_0 = 0.75$. In the absence of friction, the numerical simulation gives well-defined wrinkling, i.e., well-formed sinusoidal wrinkles of equal amplitude (Fig.S4h-j). The numerical wrinkling vanishes, however, with the addition of friction at the initial stages of pre-compression (Fig.S4e), whereby one observes the appearance of non-zero curvature at the film boundaries both numerically and experimentally (Fig.S4b,e). With increase of lateral compression, combined wrinkles with a slight localized mode in the middle (pre-crease Figs.S4g) patterns appear that resemble qualitatively the experiments (Figs.S4c-d,f-g). Consequently, at large pre-compressions and under the presence of friction, the simultaneous period-doubling and localized (pre-crease) morphology is potentially a tradeoff between the mechanical and magnetic load contributions. Further investigations should be carried out to better understand the coexistence of mechanical localized modes and magnetic wrinkles.

References

[1] A. Dorfmann and R. W. Ogden, *Eur. J. Mech. A/Solids*, 2003, **22**, 497 – 507.

[2] S. V. Kankanala and N. Triantafyllidis, *J. Mech. Phys. Solids*, 2004, **52**, 2869 – 2908.

[3] K. Danas and N. Triantafyllidis, *J. Mech. Phys. Solids*, 2014, **69**, 67 – 83.

[4] R. L. Taylor, *FEAP - Finite Element Analysis Program*, -, 2011.

[5] K. Danas, *J. Mech. Phys. Solids*, 2017, **105**, 25–53.